DØ Note 5858-CONF

Search for the Standard Model Higgs Boson in $\gamma\gamma$ final states at DØ with $L = 4.2\ fb^{-1}$ data

The DØ Collaboration
URL http://www-d0.fnal.gov
(Dated: February 24, 2009)

This note describes a search for a light Higgs boson in the di-photon final state using 4.2 ± 0.3 fb^{-1} of the DØ Run II data, collected at the Fermilab Tevatron collider from April 2002 to December 2008. Good agreement between the data and the Standard Model (SM) background prediction is observed. Since there is no evidence for new physics, we set 95% C.L. limits on the production cross section times the branching ratio ($\sigma \times BR(h \to \gamma\gamma)$) relative to the SM-like Higgs prediction for different assumed Higgs masses. The observed limits ($\sigma(limit)/\sigma(SM)$) range from 11.9 to 35.2 for Higgs mass from 100 to 150 GeV, while the expected limits range from 17.5 to 32.0.

Preliminary Results for winter 2009 Conferences

I. INTRODUCTION

In the Standard Model (SM), the $h \to \gamma\gamma$ branching ratio is small, for instance it is only 0.22% for a Higgs boson with a mass of 130 GeV. However it is well-known that the SM is incomplete. In some models beyond the SM, the $h \to \gamma\gamma$ branching ratio can be enhanced significantly, some examples can be found in Ref. [1]. The idea of the fermiophobic Higgs, which assumes zero couplings of the Higgs to the fermions, has been tested at LEP [2] - [5] and the Tevatron [6]. In this note, we update the previous 2.7 fb^{-1} results [7] using same technicals. We examine the inclusive di-photon dataset ($\gamma\gamma$+X) and search for high mass $\gamma\gamma$ resonances. The SM Higgs is used as a possible signal model, and this analysis is a forerunner to the leading low-mass Higgs analysis at the LHC [8, 9]. There are several sizeable sources of Higgs boson production within the SM. In this note, three processes: gluon gluon fusion ($gg \to H$), associated production (VH, $V = W, Z$) and vector boson fusion (VBF), are taken into account, with relative cross sections predicted by the QCD calculation. The result of the search is interpreted as upper limits on the production cross section times the branching ratio ($h \to \gamma\gamma$) relative to the SM prediction for different assumed Higgs masses.

The SM Higgs Monte Carlo (MC) samples, as well as any other MC samples used in this analysis, are generated using PYTHIA [10] with CTEQ6L [11] parton distribution functions (PDFs), and processed through a GEANT-3 based [12] simulation of the D0 detector and the same reconstruction software as the data. Samples corresponding to each of the three dominant SM Higgs boson production mechanisms discussed above are generated, and normalized using the next-to-next-to-leading order (NNLO) theoretical cross sections [13, 14] and branching ratio predictions from HDECAY [15]. The gluon fusion production cross section is also corrected for two-loop electroweak effects [16].

II. DØ DETECTOR AND DATA SAMPLE

The DØ detector is comprised of a central tracking system in a 2 T superconducting solenoidal magnet, a liquid-argon/uranium calorimeter, a central preshower detector and a muon spectrometer [17]. The major parts of the DØ detector used in event selection are the tracking system, the electromagnetic (EM) calorimeter and the central preshower detector (CPS). The tracking system consists of a silicon microstrip tracker (SMT) and an eight-layer scintillating fiber tracker (CFT) mounted on thin coaxial barrels. It provides coverage for charged particles in the pseudorapidity range $|\eta| < 3$ (where the pseudorapidity is defined as $\eta \equiv -\ln[\tan(\frac{\theta}{2})]$, with θ denoting the polar angle with respect to the proton beam direction.) The calorimeter has a central section (CC) covering up to $|\eta| \approx 1.1$, and two end components (EC) extending coverage to $|\eta| \approx 4.2$. Each section is housed in a separate cryostat, and divided into EM layers on the inside and hadronic layers on the outside. The EM calorimeter has four longitudinal layers and transverse segmentation of $0.1\times$ 0.1 in $\eta - \phi$ space (where ϕ is the azimuthal angle), except in the third layer, where it is $0.05\times$ 0.05. Immediately before the inner layer of the central EM calorimeter, there is a central preshower detector (CPS) formed of $2X_0$ of absorber followed by several layers of scintillating strips with embedded wavelength-shifting fibers. Luminosity is measured using plastic scintillator arrays located in front of the EC cryostats, covering $2.7 < |\eta| < 4.4$. The data acquisition system consists of a three-level trigger, designed to accommodate the high instantaneous luminosity. For final states containing two photon candidates with transverse momentum (p_T) above 25 GeV, the trigger efficiency is close to 100%. The data samples used in this analysis was collected between April 2002 and December 2008 and corresponds to an integrated luminosity of 4.2 ± 0.3 fb^{-1} after applying the data quality requirements.

III. EVENT SELECTION

Events are selected requiring at least two photon candidates with $p_T > 25$ GeV and $|\eta| < 1.1$, for which the trigger requirements are fully efficient. Photons are selected from EM clusters reconstructed within a cone with radius $\mathcal{R} = \sqrt{(\Delta\eta)^2 + (\Delta\phi)^2} = 0.2$ and requiring: (i) at least 97% of the cluster energy is deposited in the EM calorimeter, (ii) the calorimeter isolation variable $I = [E_{\rm tot}(0.4) - E_{\rm EM}(0.2)]/E_{\rm EM}(0.2)$ is less than 0.1, where $E_{\rm tot}(0.4)$ is the total energy in a cone of radius $\mathcal{R} = 0.4$ and $E_{\rm EM}(0.2)$ is the EM energy in a cone of radius $\mathcal{R} = 0.2$; (iii) the energy-weighted shower width squared in the $r - \phi$ plane in EM3 is less than 14 cm^2; and (iv) the scalar sum of the p_T of all tracks originating from the primary vertex in an annulus of $0.05 < \mathcal{R} < 0.4$ around the cluster ($p_{T\rm trk}^{\rm sum}$) is less than 2 GeV. To suppress electrons misidentified as photons, the EM clusters are required to not be spatially matched to tracker activity, either a reconstructed track, or a density of hits in the SMT and CFT consistent with that of an electron. The contribution of jets misidentified as photons is reduced by combining the information from a set of variables sensitive to differences between photons and jets in the tracker activity and in the energy distributions in the calorimeter and CPS, using an artificial neural network (ANN) [18]. The variables used are: $p_{T\rm trk}^{\rm sum}$, the number of cells in the first EM calorimeter layer within $\mathcal{R} < 0.2$ and $0.2 < \mathcal{R} < 0.4$ of the EM cluster, the number of associated CPS

clusters within $\mathcal{R} < 0.1$ of the EM cluster, and the squared-energy-weighted width of the energy deposition in the CPS. The ANN is trained using diphoton and dijet MC samples and its performance is verified using a data sample of $Z \to \ell^+\ell^-\gamma$ ($\ell = e, \mu$) events. Fig. 1 compares the ANN output (O_{NN}) distribution for photons and jets. Photon candidates are required to have O_{NN} larger than 0.1. Such a requirement is almost 100% efficient for photons while rejecting 50% of misidentified jets. Finally, the diphoton mass ($M_{\gamma\gamma}$), computed from the two highest p_T photons, is required to be larger than 60 GeV.

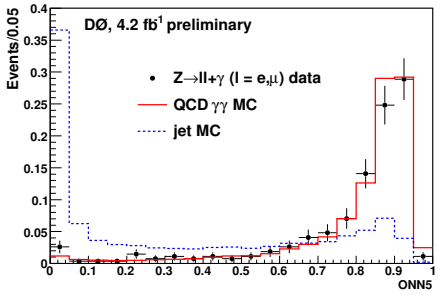

FIG. 1: Normalized distributions of O_{NN} value from real and fake photons.

IV. BACKGROUNDS

There are three major sources of background to the $h \to \gamma\gamma$ signature: (i) Drell-Yan events, where both electrons are misidentified as photons; (ii) $\gamma + jet$ and $jet + jet$ events where the jet(s) are mis-identified as photon(s); (iii) direct QCD di-photon events.

A. Drell-Yan $Z/\gamma* \to ee$ contribution

We use $Z/\gamma* \to ee$ PYTHIA MC samples to estimate the Drell-Yan contribution. The next-to-next-to-leading-order (NNLO) $p\bar{p} \to Z/\gamma* \to ee$ cross section of 254 ± 10 pb [19] for 60 - 130 GeV di-electron invariant mass region is used for the absolute normalization. From the $Z/\gamma* \to ee$ MC samples, we find that 2.0% of the electrons can satisfy the photon selection requirements described in Section III due to tracking inefficiencies. The total background contribution from the Drell-Yan process is found to be 216.3 ± 43.4 events.

B. γ+jet and di-jet background

We estimate the γ + jet and di-jet contributions from the data with the final event selection applied (see section III) by using a 4×4 matrix background subtraction method. The method is described in Ref. [20]. In this analysis, we use $O_{NN} = 0.75$ as a boundary to classify the candidates into four categories:

- N_{pp} of them have both photon candidates with $O_{NN} > 0.75$;
- N_{pf} of them have the leading photon candidate with $O_{NN} > 0.75$, but the sub-leading $O_{NN} < 0.75$;
- N_{fp} vice versa;
- N_{ff} of them have both photon candidates with $O_{NN} < 0.75$;

The Drell-Yan $Z/\gamma* \to ee$ contributions to (N_{pp}, N_{pf}, N_{fp}, N_{ff}) are determined from MC simulations and are removed. The pass-fail vector (N_{pp}, N_{pf}, N_{fp}, N_{ff}) thus obtained is related the ($N_{\gamma\gamma}, N_{\gamma j}, N_{j\gamma}, N_{jj}$) vector as follows:

$$\begin{pmatrix} N_{ff} \\ N_{fp} \\ N_{pf} \\ N_{pp} \end{pmatrix} = E \times \begin{pmatrix} N_{jj} \\ N_{j\gamma} \\ N_{\gamma j} \\ N_{\gamma\gamma} \end{pmatrix} \quad (1)$$

where the $N_{\gamma\gamma}$ is the number of γ+γ events, $N_{\gamma j}$ and $N_{j\gamma}$ are the number of γ+jet events and N_{jj} is the number of di-jet events. The 4×4 matrix E is defined as:

$$\begin{pmatrix} (1-\epsilon_{j1})(1-\epsilon_{j2}) & (1-\epsilon_{j1})(1-\epsilon_{\gamma 2}) & (1-\epsilon_{\gamma 1})(1-\epsilon_{j2}) & (1-\epsilon_{\gamma 1})(1-\epsilon_{\gamma 2}) \\ (1-\epsilon_{j1})\epsilon_{j2} & (1-\epsilon_{j1})\epsilon_{\gamma 2} & (1-\epsilon_{\gamma 1})\epsilon_{j2} & (1-\epsilon_{\gamma 1})\epsilon_{\gamma 2} \\ \epsilon_{j1}(1-\epsilon_{j2}) & \epsilon_{j1}(1-\epsilon_{\gamma 2}) & \epsilon_{\gamma 1}(1-\epsilon_{j2}) & \epsilon_{\gamma 1}(1-\epsilon_{\gamma 2}) \\ \epsilon_{j1}\epsilon_{j2} & \epsilon_{j1}\epsilon_{\gamma 2} & \epsilon_{\gamma 1}\epsilon_{j2} & \epsilon_{\gamma 1}\epsilon_{\gamma 2} \end{pmatrix} \quad (2)$$

where $\epsilon_{\gamma 1}$ and $\epsilon_{\gamma 2}$ are the fractions of the leading and sub-leading photons that have passed the event selection and have $O_{NN} > 0.75$, and ϵ_{j1} and ϵ_{j2} are the fractions of jets that have passed the event selection and have $O_{NN} > 0.75$. The photon efficiency (ϵ_γ) is estimated using direct di-photon MC and corrected for small differences between data and the simulation measured in pure samples of photon events from radiative Z decays $Z \to \ell^+\ell^-\gamma$ ($\ell = e, \mu$). The jet efficiency (ϵ_j) is estimated using di-jet MC enriched in jets misidentification as photons, and cross-checked in jet samples in data. Both efficiencies are parameterized as a function of photon pseudorapidity. ($N_{\gamma\gamma}, N_{\gamma j}, N_{j\gamma}, N_{jj}$) can be obtained by solving the linear equation. Table I shows the results after applying the method on the real data.

Total	7939
Total - N_{DY}	7722.7
$N_{\gamma\gamma}$	4538.8 $\pm$ 144.7
$N_{\gamma j} + N_{j\gamma}$	2189.0 $\pm$ 170.3
N_{jj}	994.9 $\pm$ 106.6
non-$\gamma\gamma$	3183.9 $\pm$ 200.9

TABLE I: The number of $\gamma\gamma$, γ+jet, di-jet and non-$\gamma\gamma$ (sum of γ+jet and di-jet) events in the data samples from the 4x4 matrix method. The quoted uncertainties are statistical only.

We reverse the event selection O_{NN} cut (0.1) on one of the two photon candidates to get an enriched non-$\gamma\gamma$(γ+jet,di-jet) sample from data. Fig. 2 shows that the shape of the di-photon mass distribution from such "reversed-ONN" sample is in good agreement with the results from the 4×4 matrix method. Given the good agreement between

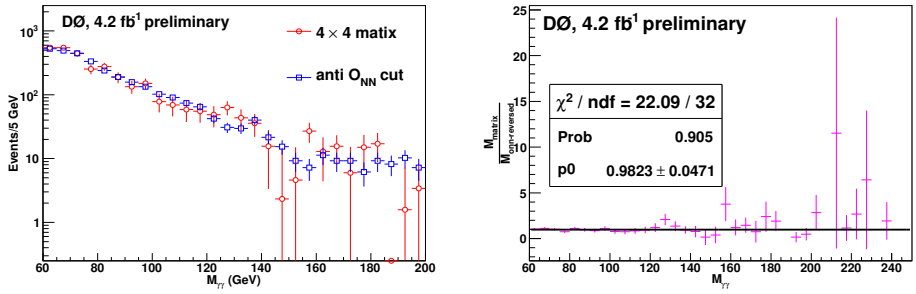

FIG. 2: non-$\gamma\gamma$ component invariant mass distribution from 4×4 matrix background subtraction and from reversing the O_{NN} cut. The area of both histograms are normalized to unity.

the distribution from the two orthogonal samples and the low statistics of the results from the matrix method, we use the "reversed-ONN" sample to determine the shape of the non-$\gamma\gamma$ background. In order to smooth out statistical fluctuations, we fit the mass distribution with an exponential function $f(M_{non}) = \exp(p_0 \cdot M_{non}^2 + p_1 \cdot M_{non} + p_2)$ with M_{non} denoting the mass of the two photon candidates. The estimation of the total number of non-$\gamma\gamma$ events from the 4x4 matrix method is used to fix the normalization. The systematic uncertainty from the shape function is taken into account when calculating the limits.

C. Direct QCD di-photon production

We obtain a di-photon invariant mass distribution (with Drell-Yan, γ+jet,di-jet subtracted off) and use the side-band fitting method to determine the QCD di-photon in the signal mass region ($M_{\rm Higgs}$-15 GeV, $M_{\rm Higgs}$+15 GeV). For each assumed Higgs mass($M_{\rm Higgs}$), we use a simple exponential function $f(M_{diem}) = \exp(p_0 \cdot M_{diem}^2 + p_1 \cdot M_{diem} + p_2)$ to fit the di-photon mass (M_{diem}) distribution in the $[70, 200]$ GeV range outside of the signal mass region ($M_{\rm Higgs}$-15 GeV,$M_{\rm Higgs}$+15 GeV). We then interpolate the function in the signal region to determine the QCD di-photon contribution.

V. SYSTEMATIC UNCERTAINTIES

The uncertainty of the $O_{NN} > 0.75$ efficiencies for the photon and photon-like jets is the main source of the uncertainty of the background subtraction. We adopt the difference in the number of background events from the mean effiencies and the upper and lower uncertainty bands as the systematic uncertainty. The influence of the parton distribution functions (PDF) uncertainty on the acceptance is 1.7% - 2.2% depending on the Higgs mass, estimated from CTEQ6M error functions. Table II lists all the systematic uncertainties of this analysis:

source	uncertainty
luminosity	6.1% [21]
trigger	0.1%
PDF for $h \to \gamma\gamma$ acceptance	1.7% - 2.2%
electron misidentification efficiency	19.0%
Z/γ^*(ee) cross section	3.9%
photon identification efficiency	6.8%
background subtraction	shape
photon energy scale	shape

TABLE II: Systematic uncertainties. The photon energy scale and background subtraction systematic uncertainties would change the signal and background shape, and are taken into account appropriately in the final limits setting.

VI. FINAL EVENT DISTRIBUTIONS AND LIMITS

A. Final event distributions

For illustration, we show the invariant mass distribution of the events in data together with those of the background estimation for the mass region [70.0 GeV, 200.0 GeV] in Fig. 3, where the Drell-Yan is estimated from MC, the non-$\gamma\gamma$ component is estimated from data by using 4×4 matrix method and the direct di-photon production is estimated from data by using side-band fitting for 130±15 GeV mass window. Figure 4 shows the final invariant mass of the

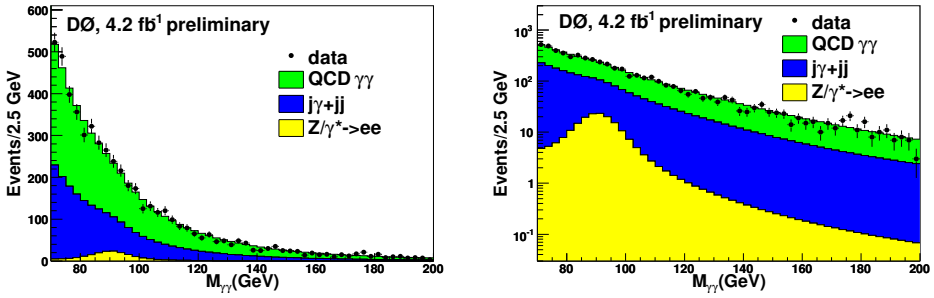

FIG. 3: Left plot shows the invariant mass distribution of two photon candidates in mass region [70.0 GeV, 200.0 GeV], right plot is the corresponding log scale distribution.

two photon candidates in the interval of ($M_{\rm Higgs}$-15 GeV, $M_{\rm Higgs}$+15 GeV) for some of the assumed Higgs mass. The shaded region corresponds to the expected background systematic uncertainty band. Table III shows the number of events in data, expected background and signal in each mass interval for different SM Higgs mass values.

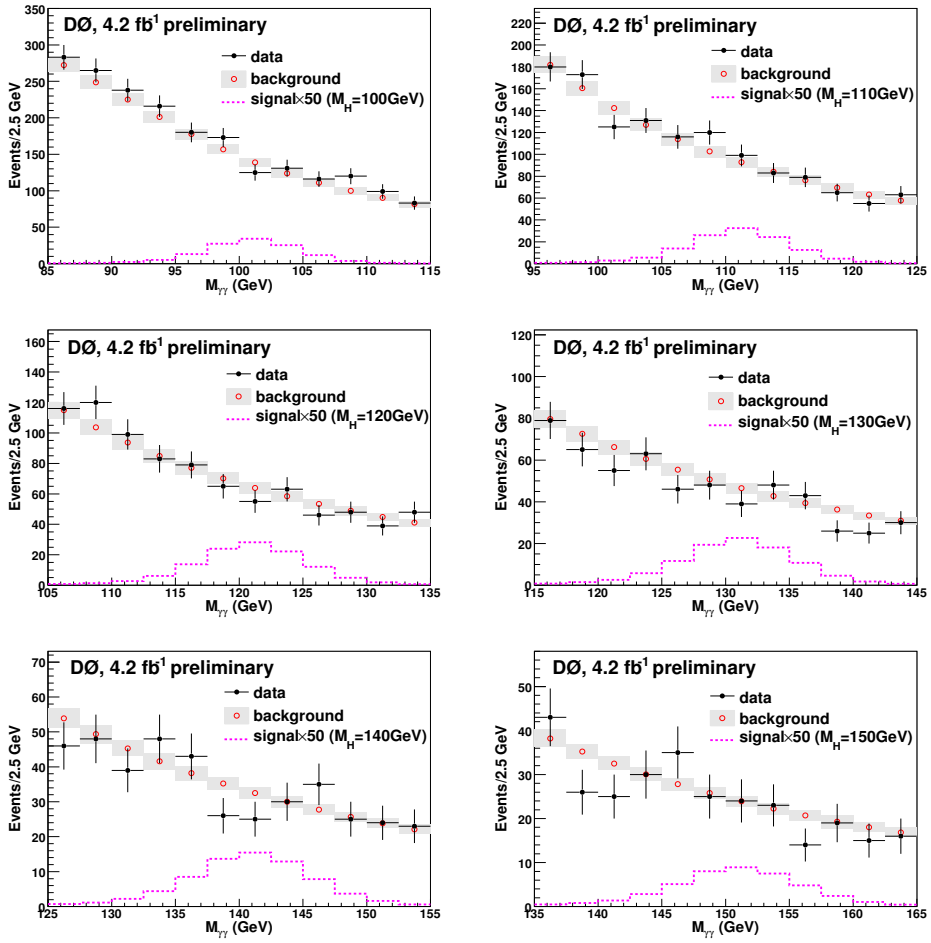

FIG. 4: Invariant mass distribution of the two photon candidates in the mass interval of ($M_{\rm Higgs}$-15 GeV, $M_{\rm Higgs}$+15 GeV) for different Higgs masses.

	100 GeV	110 GeV	120 GeV	130 GeV	140 GeV	150 GeV
ϵ_{sel}(ggH)	0.195±0.001	0.200±0.001	0.207±0.001	0.213±0.001	0.216±0.001	0.219±0.001
ϵ_{sel}(VH)	0.185±0.001	0.195±0.001	0.203±0.001	0.209±0.001	0.218±0.001	0.219±0.001
ϵ_{sel}(VBF)	0.198±0.001	0.211±0.001	0.218±0.001	0.226±0.001	0.233±0.001	0.238±0.001
$Z/\gamma* \to ee$	134±27	53±12	17±5	9±3	5±2	3±2
γj+jj	712±102	455±65	299±43	202±29	140±20	100±14
QCD γγ	1080±96	764±62	539±41	404±28	280±19	207±14
total background	1926±35	1272±21	855±14	615±10	425±7	310±5
data	2029	1289	861	567	412	295
signal	2.53±0.18	2.53±0.18	2.38±0.17	2.01±0.14	1.45±0.10	0.87±0.06

TABLE III: Event selection efficiencies(ϵ_{sel}) with their statistical errors and number of events in data, signal and the background estimation in the mass interval of ($M_{\rm Higgs}$-15 GeV, $M_{\rm Higgs}$ + 15 GeV) from 100 GeV to 150 GeV in 10 GeV step, where the systematic uncertainties have been included for both signal and background, the correlation between the different backgrounds has been considered when calculating the error for the total background.

B. Limit setting

Since there is no excess observed above the background expectation, we proceed to set upper limits on the Higgs production cross section times branching ratio for Higgs decaying into a pair of photons. The distributions of invariant mass of the two photon candidates in the interval of ($M_{\rm Higgs}$-15 GeV, $M_{\rm Higgs}$ + 15GeV) (shown in Fig. 4) are used for this purpose. Limits are calculated at the 95% confidence level using the modified frequentist CLs approach with a Poisson log-likelihood ratio test statistic [22, 23]. The impact of systematic uncertainties is incorporated via convolution of the Poisson probability distributions corresponding to the different sources of systematic uncertainty. The correlation in systematic uncertainties are maintained between signal and backgrounds. In this analysis, we use the diphoton invariant mass as the discriminant for limits setting. We find that the selection efficiency varies smoothly and the di-photon mass resolution is almost constant (3 GeV). Therefore, we are able to determine the limits also in every 2.5 GeV mass values by interpolation of the efficiencies and mass distributions of the signal using MC samples generated at every 5 GeV mass points. Table IV shows the limits on $\sigma \times BR$ for the different Higgs masses. Table V shows the limits on $\sigma \times BR$ relative to the SM prediction for different Higgs masses. The corresponding graphs are displayed in Fig. 5.

Higgs mass (GeV)	100	102.5	105	107.5	110	112.5	115	117.5	120	122.5	125	127.5	130	132.5	135	137.5	140	142.5	145	147.5	150
observed limits (fb)	93.9	98.4	102.9	108.5	86.1	68.8	46.3	38.1	36.0	35.3	30.0	30.5	29.4	30.9	30.6	27.2	26.7	30.5	33.2	33.4	27.0
expected limits (fb)	74.5	69.6	66.1	61.9	58.1	55.8	53.9	51.6	48.1	46.8	45.2	43.6	41.0	40.4	38.3	37.2	34.3	34.1	32.2	31.7	29.7

TABLE IV: 95% C.L. limits on $\sigma \times BR$ for the different Higgs masses.

Higgs mass (GeV)	100	102.5	105	107.5	110	112.5	115	117.5	120	122.5	125	127.5	130	132.5	135	137.5	140	142.5	145	147.5	150
observed limits	29.7	31.4	33.0	35.2	28.3	22.9	15.8	13.3	13.1	13.2	11.9	12.6	13.1	14.6	16.0	15.2	16.9	21.2	26.8	30.1	29.1
expected limits	23.6	22.2	21.2	20.1	19.1	18.6	18.5	18.0	17.5	17.6	17.9	18.0	18.3	19.1	20.0	20.8	21.7	23.6	25.9	28.5	32.0

TABLE V: 95% C.L. limits on $\sigma \times BR$ relative to the SM prediction for different Higgs masses.

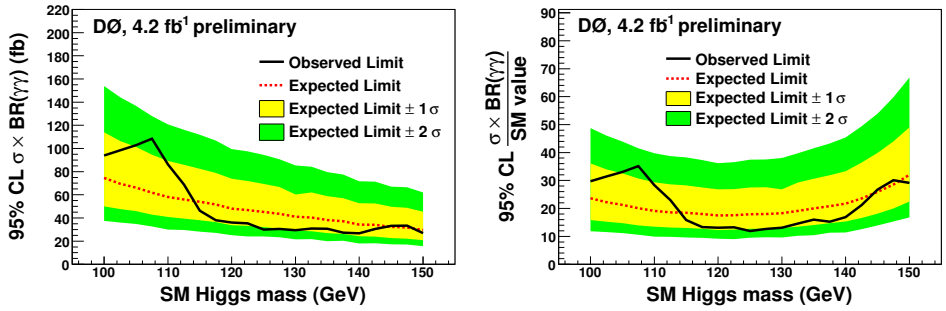

FIG. 5: 95% C.L. limits on the $\sigma \times BR$ (left) and on the $\sigma \times BR$ relative to the SM prediction as a function of Higgs mass.

VII. SUMMARY

This note describes a search for the SM Higgs boson in the di-photon channel in 4.2 fb^{-1} DØ Run II data. The data and SM background estimation are consistent, so we set the 95% C.L. limits on the $\sigma \times BR$ relative to the SM prediction for different SM Higgs masses. The observed limits ($\sigma(limit)/\sigma(SM)$) are from 11.9 to 35.2 for Higgs mass from 100 to 150 GeV, while the expected limits range from 17.5 to 32.0. By comparsion with the 2.7 fb^{-1} results [7], the limits are improved by about 20%, which is little lower than the luminosity increase.

Acknowledgments

We thank the staffs at Fermilab and collaborating institutions, and acknowledge support from the DOE and NSF (USA); CEA and CNRS/IN2P3 (France); FASI, Rosatom and RFBR (Russia); CAPES, CNPq, FAPERJ, FAPESP and FUNDUNESP (Brazil); DAE and DST (India); Colciencias (Colombia); CONACyT (Mexico); KRF and KOSEF (Korea); CONICET and UBACyT (Argentina); FOM (The Netherlands); STFC (United Kingdom); MSMT and GACR (Czech Republic); CRC Program, CFI, NSERC and WestGrid Project (Canada); BMBF and DFG (Germany); SFI (Ireland); The Swedish Research Council (Sweden); CAS and CNSF (China); and the Alexander von Humboldt Foundation.

[1] S. Mrenna and J. Wells, arXiv:hep-ph/0001226, (2000).
[2] A. Heister et al. (ALEPH Collaboration), Phys. Lett. B **544**, 16 (2002).
[3] P. Abreu et al. (DELPHI Collaboration), Phys. Lett. B **507**, 89 (2001); Eur. Phys. J. C **35**, 313, (2004).
[4] G. Abbiendi et al. (OPAL Collaboration), Phys. Lett. B **544**, 44 (2002).
[5] P. Achard et al. (L3 Collaboration), Phys. Lett. B **534**, 28 (2002); Phys. Lett. B **568**, 191 (2003).
[6] DØ Collaboration, "Search for Light Higgs Boson in $\gamma\gamma$+X Final State with the DØ Detector at $\sqrt{s}$ = 1.96 TeV", DØ Note **5426-CONF** (2007).
[7] DØ Collaboration, arXiv.org:0901.1887, (2009).
[8] ATLAS Calorimeter Performance, TDR-1, CERN/LHCC 96-40, December 1996.
[9] CMS ECAL Technical Design Report, CERN/LHCC 97-33, CMS TDR 4, 15 December 1997.
[10] T. Sjöstrand *et al.*, Comput. Phys. Commun. **135**, 238 (2001).
[11] H.L. Lai *et al.*, Phys. Rev. D **55**, 1280 (1997).
[12] R. Brun and F. Carminati, CERN Program Library Long Writeup W5013, 1993 (unpublished).
[13] S. Catani *et al.*, JHEP **0307**, 028 (2003).
[14] K.A. Assamagan *et al.*, arXiv:hep-ph/0406152 (2004).
[15] A. Djouadi, J. Kalinowski and M. Spira, Comput. Phys. Commun. **108**, 56 (1998).
[16] U. Aglietti *et al.*, arXiv:hep-ph/0610033 (2006).
[17] V. M. Abazov *et al.*, Nucl. Instrum. Meth. A **565**, 463 (2006).
[18] C. Peterson, T. Rognvaldsson and L. Lonnblad, "JETNET 3.0 A versatile Artificial Neural Nertwork Package", Lund University Preprint LU-TP 93-29. Version 3.5 is used here.
[19] R. Hamberg, W. L. van Neerven and T. Matsuura, Nucl. Phys. B **359**, 343 (1991) [Erratum-ibid. B **644**, 403 (2002)].
[20] Y. Liu, Ph.D. thesis, Fermilab [FERMILAB-THESIS-2004-37] (2004).
[21] T. Andeen *et al.*, FERMILAB-TM-2365 (2007).
[22] W. Fisher, FERMILAB-TM-2386-E (2006).
[23] T. Junk, Nucl. Intrum. Meth. A **434**, 435 (1999); A. Read, CERN 2000-005 (30 May 2000).
[24] http://maltoni.web.cern.ch/maltoni/TeV4LHC/SM.html .